In situ time resolved wide angle X-Ray diffraction study of nanotube carpet growth: nature of catalyst particles and progressive nanotube alignment

Périne Landois, Mathieu Pinault, Stéphan Rouzière, Dominique Porterat, Cristian Mocuta, Erik Elkaim, Martine Mayne-L'Hermite, Pascale Launois

In situ time resolved wide angle X-ray diffraction study of nanotube carpet growth: Nature of catalyst particles and progressive nanotube alignment

Périne Landois[a,b,1], Mathieu Pinault[b], Stéphan Rouzière[a], Dominique Porterat[b], Cristian Mocuta[c], Erik Elkaim[c], Martine Mayne-L'Hermite[b,*], Pascale Launois[a,*]

[a]Laboratoire de Physique des Solides, UMR CNRS 8502, Université Paris Sud, F-91405 Orsay Cedex, France

[b]CEA, IRAMIS, UMR-3685 NIMBE LEDNA, F 91191 Gif-sur-Yvette, France, CNRS, UMR-3685 NIMBE, F 91191 Gif-sur-Yvette, France

[c]Synchrotron SOLEIL, L'Orme des merisiers, Saint Aubin, Gif-sur-Yvette FR91192, France

Catalytic chemical vapor deposition is the most promising process to obtain vertically aligned carbon nanotube (VACNT) carpets. Live analysis of growing VACNT is crucial to reveal their nucleation and growth mechanisms. We present novel time resolved *in situ* X-ray diffraction (XRD) analysis on growing macroscopic VACNT carpets enabling us to get statistical information on catalytic phase together with nanotube progressive alignment. A specific synthesis set-up has been developed to perform such *in situ* synchrotron XRD experiments. Nucleation kinetics of the different phases are evidenced: first, orthorhombic Fe_3C crystalline phase is formed, followed by the formation of CNTs and finally of γ-Fe, demonstrating that Fe_3C particles are the nucleation seeds for CNT growth. The additional formation of Fe_3C or γ-Fe nanowires inside CNTs is associated with capillary forces and mobility of them at 850 °C. Experiments also reveal the progressive formation and alignment of VACNT carpets during the continuous precursor injection. Quantification of the alignment degree allows one to get a better understanding of the effect of precursor injection rate and CNT length on VACNT alignment. The overall results are key issues for the scaling-up of VACNT synthesis and their applications towards commercialization.

1. Introduction

Vertically-aligned carbon nanotubes (VACNT) carpets are promising nano-structured networks for a large range of applications [1] such as filtration [2,3], or in integrated circuits [4] and composite materials [5,6]. Significant improvements have been obtained in terms of synthesis of such networks, this being related to the versatility of the processes enabling to get either multi-walled CNT (MWCNT) carpets [7,8] or single-walled CNT carpets [9–12] with high growth rates (several tenth of μm/min). Thermal catalytic chemical vapor deposition (CCVD) processes are the preferred methods to produce VACNT because they are simple, efficient and low cost processes. Among them, two alternatives have been developed to synthesize VACNT, depending on how the catalyst nanoparticles used for the growth of nanotubes are prepared.

* *Corresponding authors.*
E-mail addresses: martine.mayne@cea.fr (M. Mayne-L'Hermite), pascale.launois@u-psud.fr (P. Launois).
[1] Current address: Laboratoire Charles Coulomb, UMR CNRS 5221, Université Montpellier II, Montpellier Cedex 5, FR 34095, France.

The pre-deposition by physical deposition processes of a catalyst layer on a substrate involves a two-step process while the *in situ* formation of catalyst nanoparticles from a metal precursor fed in the reactive gas used for VACNT synthesis corresponds to a one-step process. This last one, generally reported in the literature as aerosol-assisted or direct liquid injection CVD processes (AACCVD and DLICVD respectively) and operated at atmospheric pressure, requires simple equipment with no need for vacuum systems [13], which makes it rather simple to operate and suitable for VACNT fast and continuous production at a lower cost as compared to the two-step CVD process [14].

In order to control and to further improve or extend the one-step CVD synthesis process, it is crucial to study how VACNT carpets are growing through this process, in terms of nature of catalyst particle governing CNT nucleation as well as of growth and nanotube alignment. *In situ* growth monitoring by either global or local techniques (according to the size scale analyzed) is a very powerful approach since it allows obtaining instantaneous information while nanotubes are growing. Different techniques have been used to study *in situ* CNT growth whatever CNT arrangement (random or aligned): environmental microscopy techniques [15–18], surface analysis techniques [15,18–22] and structure analysis techniques [18,23–29]. Only few studies regarding *in situ* analysis of VACNT growth are reported in a CVD reactor operated at the laboratory scale [24,25,27,28], in conditions which are representative for large scale production of macroscopic VACNT samples. Moreover, to the best of our knowledge, none of them are dealing with VACNT synthesized through a one-step CVD process. In the previous *in situ* XRD studies of VACNT growth [24,25], the time resolution was about few minutes which made impossible the monitoring of VACNT growth in real time. Later, by improving time resolution, the instantaneous VACNT growth rate was determined by laser reflectometry [28]; catalyst nanoparticle size as well as CNT alignment during VACNT growth were measured by time resolved GISAXS (resolution time: 10 ms) [27]. Time resolved *in situ* studies of VACNT macroscopic samples grown by the one-step CVD process involving the formation of both catalyst nanoparticles and nanotubes from precursors injected in the gas phase, in a CVD reactor at the laboratory scale, are still missing. Covering this gap is the object of the present study.

In this paper, we present results obtained using time resolved wide angle X-ray scattering (WAXS) technique implemented on an AACCVD prototype equipment, allowing to grow rapidly and continuously vertically aligned multi-walled carbon nanotubes from catalyst particles generated from organometallic precursor (ferrocene), in conditions similar to the ones operated at the laboratory scale [30,31]. The objective was to determine, during such a one-step VACNT CVD growth, the formation kinetics and the nature of the metal-based catalyst particles during VACNT nucleation and growth stages, together with the changes in the organization of the nanotube anisotropic network. We demonstrate, during VACNT macroscopic carpet synthesis, the *in situ* formation of orthorhombic Fe_3C crystalline phase which is at the origin of VACNT growth. Simultaneously, we were able to follow quantitatively the CNT progressive alignment depending on the precursor injection rate. This innovative approach, both in terms of the method used (WAXS) and of the one-step synthesis process studied, brings new information on the nature and structure of metal-based particles at the basis of the CNT and inside, as well as on the parameters governing nanotube orientation, in the case of AACCVD synthesis process which exhibits real industrial potentialities.

2. Experimental

Vertically aligned multi-walled carbon nanotube (VA-MWCNT) carpets were synthesized by AACCVD. Both carbon (toluene) and catalytic (ferrocene) precursors are injected simultaneously and continuously into a specific reactor coupled to a CVD furnace specifically developed for synchrotron beamline experiments [32]. The stainless steel reactor (Fig. 1) has been specifically designed with Kapton® windows transparent to X-rays. The internal surfaces of the windows are flushed with helium gas in order to avoid any VACNT growth on the window surface. The VACNT sample grows on a 10 μm thick silicon wafer located at the center of the heated area of the furnace (Fig. 1 inset). An X-ray prototype

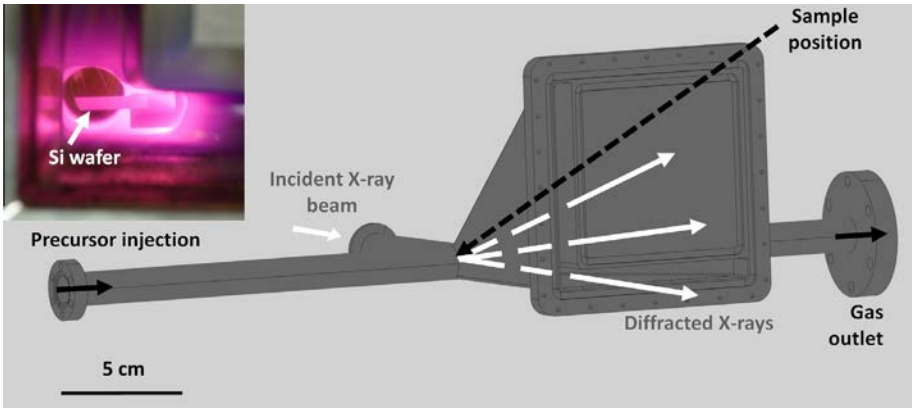

Fig. 1 – Schematics of the specific reactor developed to perform XRD experiments on synchrotron beam-lines showing the sample position in the reactor relative to X-ray beam and precursor injection. Inset: photograph of the Si substrate placed in the middle of the hot furnace at 850 °C just before the aerosol injection. (A color version of this figure can be viewed online.)

hybrid pixel area detector (XPAD) [33,34] is collecting the X-ray intensity scattered through an 'L' shape exit window [32]. As it will be shown later, this specific shape of the window enables one to record XRD patterns in two directions, along and perpendicularly to the CNT preferential growth axis (Fig. 2(a)). Thanks to the very high sensitivity of the detector and the intense synchrotron X-ray beam, fast data acquisition rate (0.5 Hz frequency) could be chosen, whilst having a good signal/noise ratio. XRD experiments were carried out at Synchrotron SOLEIL on CRISTAL beam line with photons of 17.1 keV energy, giving access to a wide Q-range (up to 5 $Å^{-1}$). Beam size is 0.8 mm (horizontally) × 0.2 mm (vertically) for full width at half maximum (FWHM), which enables to analyze the entire volume of the growing VACNT macroscopic carpet and thus a significant population of nanotubes. The rapid acquisition (1 s) is crucial to identify by WAXS the

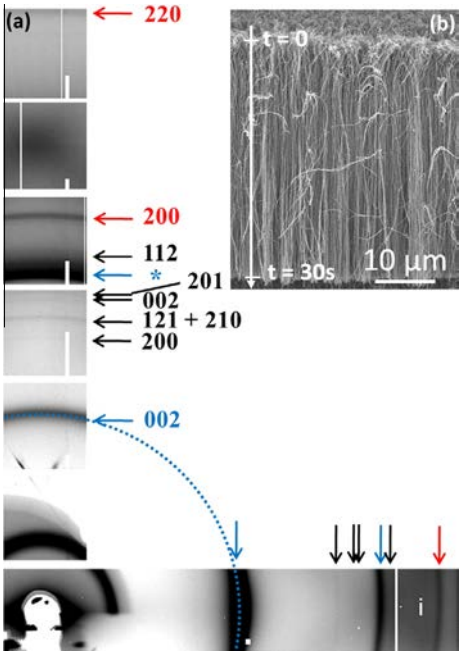

Fig. 2 – (a) Scattering pattern (1 s exposure) obtained from raw data, measured at 850 °C after 30 s of injection of the aerosol for a high injection rate (0.53 g/min). The grayscale image represents the logarithm of the intensity values, low and high intensities corresponding respectively to white and black color levels. The X-ray beam was passing through the plane of the silicon wafer which was placed horizontally. The image area is determined by the L-shaped exit window of the furnace; the rest of the detector image is not shown (no scattered X-ray). Note the presence of the 002 CNT scattering peak (blue arrows and dotted circle), of Fe_3C (black arrows) and γ-Fe (red arrows) ones.* Refers to unresolved 10 peak of CNT, where the two indices 10 are the Miller indices of two-dimensional graphene forming the CNT walls, plus 211, 102, 220 and 031 peaks of Fe_3C, plus 111 peak of γ-Fe. The silicon wafer was horizontal. (b) *Ex situ* scanning electron microscopy observation of the corresponding sample, exhibiting a preferential alignment perpendicular to the Si substrate surface. (A color version of this figure can be viewed online.)

catalyst nanoparticle nature and structure, together with changes in the alignment degree during both the VACNT nucleation and growth steps. Syntheses were performed at 850 °C by injecting the precursor (toluene/2.5 wt% of ferrocene) at two different rates (high (0.53 g/min) and low (0.27 g/min)) in order to evaluate the effect of the growth kinetics on the occurrence of the different phases and on alignment of CNT.

Scanning electron microscopy (SEM) *ex situ* observations have been performed in order to validate the new experimental CVD prototype set-up and to determine the VACNT carpet thickness. After 30 s of injection (at high rate), a 40 μm thick VA-MWCNT carpet is formed at the surface of the Si wafer (Fig. 2(b)), which is similar to carpets previously obtained with the same process using laboratory CVD equipment [30,31]. It is important to note the absence of iron-based particles located between and on VACNT in the carpet: such particles are in fact located at the base or inside CNT, as reported previously [35,36] and also shown later (Fig. 4(d) and (e)). In addition, there is no nanotube growing on VACNT surface. Indeed, CNT are grown through a base growth mechanism [30,35] for which iron-based nanoparticles formed from homogeneous nucleation in the gas phase [31] are deposited on the substrate surface and remain located at CNT base [30,35].

3. Results and discussion

Results concerning the kinetics of appearance and the identification of the different iron-based phases together with changes of CNT alignment degree during the VACNT nucleation and growth steps are presented and discussed in the following sections.

3.1. *Kinetics of appearance and identification of the different crystalline phases*

Diffraction pattern acquired for a 30 s injection of a toluene/ferrocene (2.5 wt%) aerosol mixture at high injection rate in the dedicated reactor heated at 850 °C is presented in Fig. 2(a). It consists of concentric diffraction rings characteristic of CNT and of iron-based phases located inside CNT or at their base [35,36]. The 002 ring (dotted portion of blue circle) at 1.81 $Å^{-1}$ is characteristic of the diffraction from the regularly spaced CNT walls [36]. Regarding iron-based phases, one can clearly identify diffraction rings attributed to orthorhombic cementite Fe_3C and to face-centered cubic (fcc) γ-Fe crystalline phases (black and red arrows in Fig. 2(a), respectively) [36]. Slight modifications with respect to room temperature peak positions are attributed to temperature.

XRD diagrams $I(Q)$, where I is the scattered intensity and Q the scattered wave-vector, are extracted from the recorded patterns and reported for different acquisition times (every 2 s) in Fig. 3 (see also the movie in Supplementary material and Fig. S1). They give clear evidence of the order of appearance of the different phases. For high precursor injection rate (0.57 g/min, synthesis duration: 30 s), a peak at 3.10 $Å^{-1}$ (Figs. 3(a) and S1) is first observed after 8.2 s of injection and an additional peak at 2.63 $Å^{-1}$ appears 2 s later. Both diffraction peaks are characteristic of cementite, their sequential appearance being related to their relative intensities. At

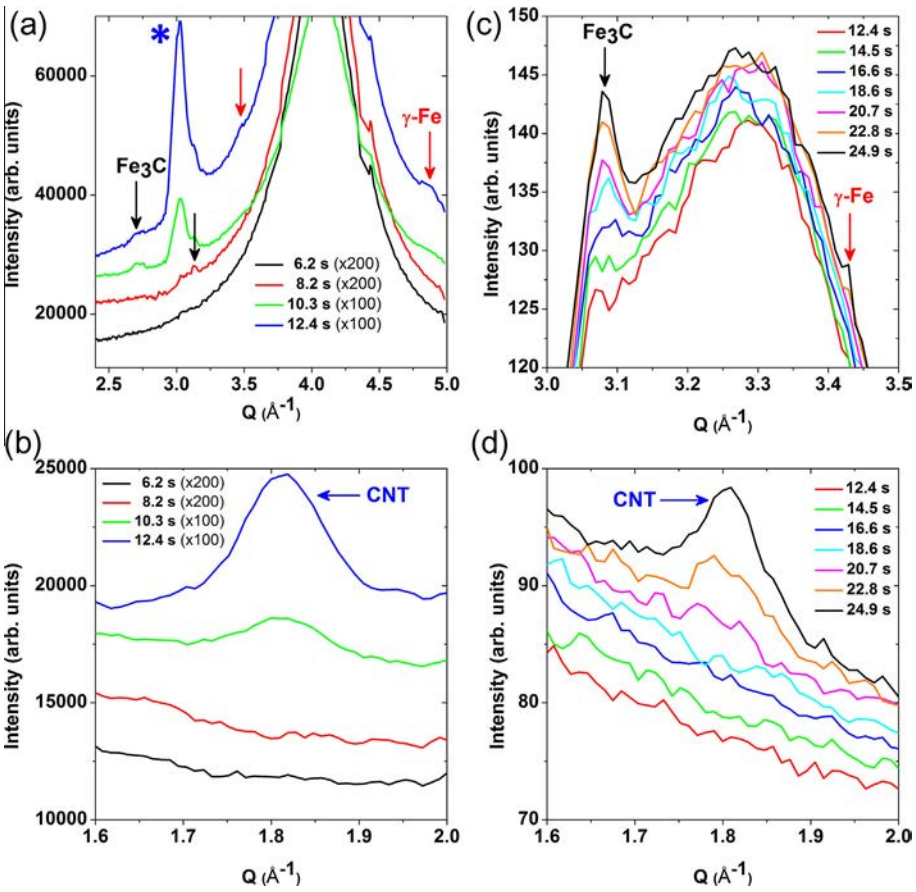

Fig. 3 – XRD diagrams obtained during the early steps of the precursor injections for the high ((a) and (b)) or low ((c) and (d)) injection rates (0.53 and 0.27 g/min, respectively). Times t are relative to the beginning of injection which corresponds to t = 0. Characteristic diffraction peaks of CNT, orthorhombic cementite Fe_3C and cubic face centered γ-Fe are indicated. The star refers to unresolved peaks of CNT, Fe_3C and γ-Fe. Curves are translated vertically for the sake of clarity. Fig. S1 is another representation of figure 3(a) with the same abscise axis as in figure 3(c) in order to better reveal the Fe_3C XRD peak. (A color version of this figure can be viewed online.)

t = 10.3 s from the beginning of the injection, a peak at 1.81 $Å^{-1}$, originating from diffraction by MWCNT, is detected (Fig. 3(b)). Approximately 2 s later (t = 12.4 s, Fig. 3(a)), new peaks at 3.45 and 4.87 $Å^{-1}$, corresponding to the fcc γ-Fe, are detected. For low precursor injection rate (0.27 g/min, synthesis duration: 60 s), the same kinetics of appearance is observed for the different phases but with a shift towards longer times as compared to the synthesis operated at high injection rate. A well-defined peak at 3.10 $Å^{-1}$, characteristic of Fe_3C, occurs at t = 18.6 s (Fig. 3(c)), and 4 s later (at t = 22.8 s), an additional peak at 1.81 $Å^{-1}$ corresponding to CNT is observed (Fig. 3(d)). Finally, γ-Fe peak at 3.45 $Å^{-1}$ appears 24.9 s after the beginning of the injection. Whatever the injection rate, the times characteristic of Fe_3C appearance are compatible with the duration necessary for the reactive gaseous species to reach the center of the reactor where the analyzed sample is placed (see additional experimental details in Appendix A).

In order to follow more quantitatively the changes of the amount of each phase all along the precursor injection duration, the intensity of the iron-based phases and CNT peaks, recorded along lines on the detector and integrated in Q, is drawn as a function of time on Fig. 4. For low precursor injection rate, intensity of Fe_3C peak increases rapidly from 18.6 s injection time and reaches a plateau at 22.8 s (Fig. 4(a)). From this moment (22.8 s), the CNT peak intensity starts to increase (Fig. 4(a)) while the γ-Fe peak appears later (Fig. 4(b)). Contrary to the Fe_3C peak intensity which reaches a plateau, indicating a constant Fe_3C amount, both the CNT and γ-Fe peak intensity increase progressively all along the precursor injection duration. For high injection rate (Fig. 4(c)), a substantial difference is found with a progressive increase of the Fe_3C peak intensity during all injection (Fig. 4(c)). Note that the slight increase of peak intensities for a few seconds after the end of the precursor injection (Fig. 4(a) and (c)) is explained by the presence of a residual atmosphere in the reactor containing both carbon and iron-based precursors. This time scale is compatible with the complete evacuation of the precursor vapor of the reactor (see additional experimental details in Appendix A).

To summarize, based on time-resolved WAXS experiments, we established the kinetics of appearance of the different crystalline phases formed during the synthesis of macroscopic VACNT samples in a CVD reactor. Whatever the precursor injection rate, orthorhombic Fe_3C crystalline

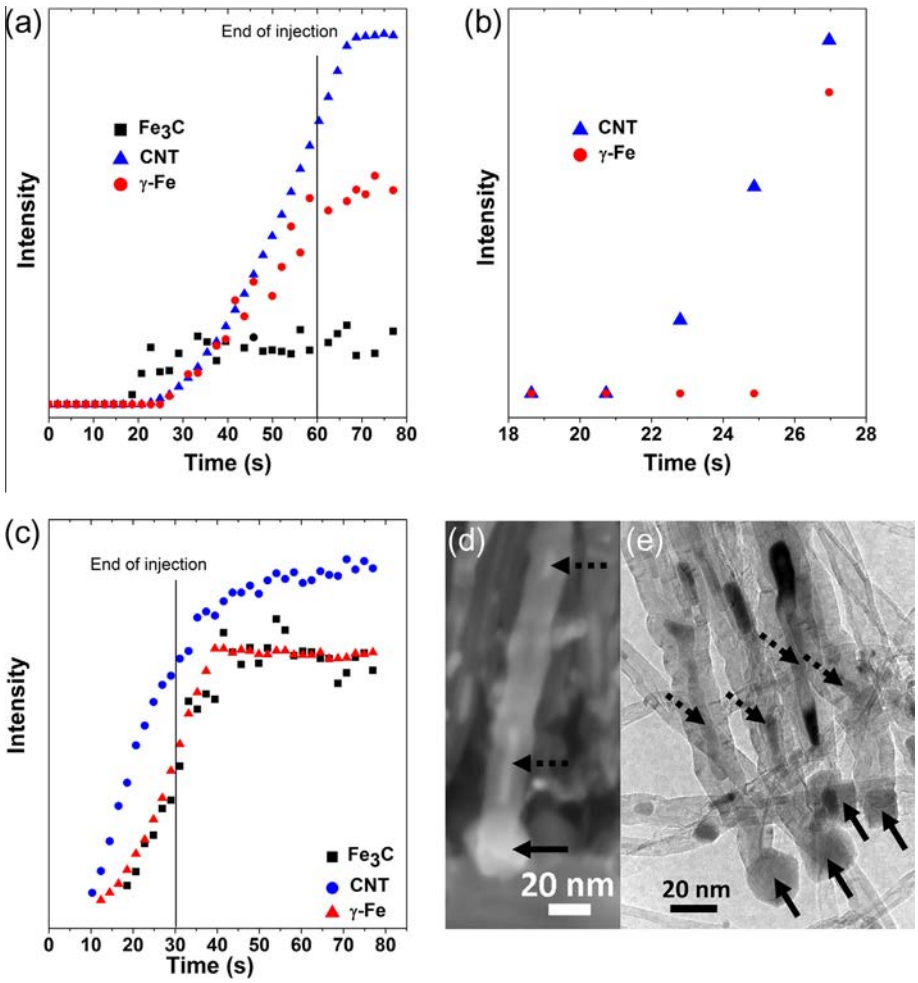

Fig. 4 – Intensities of 002 CNT, 200 γ-Fe and 112 Fe_3C peaks versus time starting from the beginning of precursor injection (time 0), for injection duration of roughly (a and b) 60 s with the low injection rate (0.27 g/min) and (c) 30 s with the high injection rate (0.53 g/min). (b) Is a zoom of (a) around the first non-zero values of the 002 CNT. Intensities are renormalized for the sake of clarity. *Ex situ* (d) SEM and (e) TEM observations of the base of the CNT carpet located at the surface of the Si substrate showing the iron-base particle at the origin of the CNT growth (full arrows) and nanowires in the CNT cores (dotted arrows). These images were performed for samples synthesis at low injection rate (0.27 g/min); similar ones were obtained at high injection rate (0.53 g/min). (A color version of this figure can be viewed online.)

phase is first formed, then CNT are formed, which is followed by the formation of the fcc γ-Fe phase. It should be underlined that whatever the precursor injection rate, no evidence for liquid phase nanoparticles is found: (i) no additional phase appears upon cooling from 850 °C to 550 °C and (ii) the same XRD results have been obtained at lower synthesis temperature (780 °C).

In order to analyze into more details the catalyst particle and nanotube nucleation step, low precursor injection rate experiments are particularly interesting, involving a decrease in CNT growth rate and lower formation kinetics for all phases. The occurrence of the iron carbide characteristic peak before the 002 peak of CNT, in conjunction with the saturation of its intensity before CNT growth, is a strong indication that this phase is at the origin of CNT formation. Ferrocene vapor is thermally decomposed giving rise, through homogeneous nucleation, to iron-based particles formed in the gas phase; such particles are subsequently deposited on the reactor walls or on substrates due to collision with the wall or substrate surfaces [31]. From these nanoparticles, toluene is then catalytically decomposed and CNT grow through a base-growth mechanism [31,36]. According to the precursor contents injected in the reactor, the reactive gaseous atmosphere is C-rich as compared to iron (99.2 wt% of carbon and 0.8 wt% of iron). Even if it is difficult to directly refer to the Fe-C phase diagram since a gas phase is involved in our synthesis, the chemical conditions used here correspond to the area, in the phase diagram, in which C content is higher than 6.67 wt% leading to the formation of iron carbide (Fe_3C) and carbon. Other studies also reported the formation of Fe_3C from gaseous precursors [38,39] and some others point out that, during metal dusting, for high carbon content in the gaseous carbon source, only carbides are formed [40,41]. These arguments explain Fe_3C cementite formation, as the first crystalline phase identified, in our synthesis conditions.

With respect to the information found in the literature, we note that the occurrence of iron carbide together with CNT in samples synthesized by CVD methods has already been reported either through characterizations of carbon filaments in the eighties [42–44] or more recently through physico-chemical analysis of CNT [45–47]. It has even been reported through *in situ* studies of CNT growth [17,24,25,29] or CNT heat treatment or electron irradiation [16,49]. In these studies, iron carbide is found to play either a role of catalyst [17,24,29,42,43,45,48] or a role of intermediate phase [25,44,47] for the formation of carbon filaments or nanotubes. In addition, even if iron carbide is reported together with CNT, in some cases, additional phases are also reported [24,25,45–47,48] but without any indication on the kinetics of appearance of each phase. More particularly, in the case of *in situ* analysis of CNT growth, apart for *in situ* local analysis (TEM) for which acquisition time is sufficiently small (0.35 s for instance for Yoshida et al. [17]), for the other techniques involving global analysis (in terms of size scale), and in particular XRD, the acquisition time is too high (from few min to tenth of min in the case of Nishimura et al. and Emmenegger et al. [24,25]). Following precisely the time evolution of each phase, in a statistical way as it is the case with XRD, constitutes an innovative experimental approach and gives undeniably a major piece of information to clarify the role of Fe_3C in CNT formation. Moreover, *in situ* WAXS acquisitions reveal the absence of iron oxide phases which, on the contrary, are observed in *ex situ* analysis [36], thus confirming the importance of *in situ* analysis to identify clearly the phase at the origin of CNT nucleation and growth.

The role of metal carbides in the synthesis of various forms of carbon nanotubes is still a matter of debate [49]. Two major hypothesis regarding the role of iron carbide as catalyst or intermediate phase are reported: (i) either iron carbide is considered to be stable and then CNT are formed from supersaturated solutions [48,49] (ii) or iron carbide exposed to carbon species originating from hydrocarbon decomposition decomposes into metallic iron and graphite [25,50], a process known as metal dusting in steel making industry [40]. In the case of high carbon concentration, the transformation involves the formation of γ-iron [51]. In our VACNT synthesis by AACCVD, whatever the precursor injection rate, γ-Fe is the last crystalline phase occurring during CNT growth step. One of the raised questions is to identify its location and to understand the origin of its formation and its role, if any, in VACNT nucleation and growth. Regarding the location of the different iron-based phases, SEM (Fig. 4(d)) and TEM (Fig. 4(e)) *ex situ* observations of our samples were performed at the base of the carpet next to the Si substrate surface in order to check if the catalyst particles are located at the CNT base since a base growth mechanism was already demonstrated for VACNT grown by AACCVD [30]. Using the different chemical contrast between carbon and metal, electron microscopy observations confirm the presence of catalyst nanoparticles at the base of each CNT (full arrow) as well as that of nanoparticles and nanowires encapsulated in their hollow core (dotted arrows in Fig. 4). This is the result of the continuous feeding with fresh formed metal-based nanoparticles in the gas phase [31] during the whole synthesis duration, implying a continuous enrichment and growth of the catalyst particles and subsequently the detachment of metal-based nanowires lifted up inside CNT [52]. For the low precursor injection rate, since the amount of the Fe_3C phase is constant before and all along CNT growth, one can assume, according to the base growth mechanism identified, that this phase is located at the CNT base and is definitely the phase responsible for VACNT nucleation and growth in our conditions of AACCVD process. Then, particles at CNT base are continuously fed with carbon and iron species involving the continuous formation of Fe_3C and CNT. The constant quantity of Fe_3C measured for low precursor injection rate indicates that equilibrium between Fe_3C formation and Fe_3C decomposition into γ-Fe and C is established. Because of the mobility of iron-based particles at this temperature (850 °C) [17,45,53] and of the capillary forces inside the growing CNT [49,54], the particles at CNT base separate leaving the mother particle at CNT base and forming γ-Fe nanowires rising inside CNT (Fig. 5), as shown by the progressive increase of γ-Fe quantity all along CNT growth observed in *in situ* time resolved WAXS experiment. As Fe_3C exposed to carbon species is decomposed into γ-Fe and graphite, it is most probable that Fe_3C particle at CNT base is surrounded by a thin layer of γ-Fe at the Fe_3C/CNT interface as drawn in Fig. 5 [26,50,55]. However, such a layer is difficult to detect by XRD. For low precursor injection rate, involving slow CNT growth, the Fe_3C transformation kinetics is compatible with the CNT growth rate meaning that Fe_3C complete transformation is possible before the detachment of nanowires from nanoparticles at CNT base and their lift-up inside CNT. This corroborates the occurrence of iron carbide nanoparticles at CNT base and of γ-iron nanowires inside CNT.

Similar reasoning can be applied to the high injection rate with the difference that iron carbide phase is both located at the CNT base and inside CNT. Indeed, the intensity of Fe_3C peak is increasing as the intensity of CNT peak increases (Fig. 4(c)). Contrary to the low injection rate case, CNT growth is fast and the Fe_3C transformation kinetic is lower than CNT

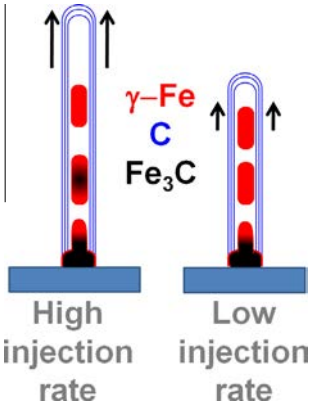

Fig. 5 – Schematic representation of the MWCNT and iron-based phases for low and high injection rates (0.27 and 0.53 g/min, respectively). For the low precursor injection rate, Fe_3C phase is located at the CNT base while nanowires inside CNT are γ-Fe nanowires. For the high precursor injection rate, both Fe_3C and γ-Fe are present inside CNT. (A color version of this figure can be viewed online.)

growth rate meaning that Fe_3C complete transformation is not possible before the detachment of nanowires from nanoparticles at CNT base and their lift-up inside CNT. This explains the occurrence of iron carbide both at CNT base and entrapped inside CNT. Then, the Fe_3C nanowires entrapped can be partly decomposed into γ-Fe and graphite, resulting in the presence of both Fe_3C and γ-Fe phases inside CNT (Fig. 5(b)), as previously determined through *ex situ* analysis [36]. Therefore, in both cases (high and low injection rate), γ-Fe cannot be the phase at the origin of the formation of CNT. For comparison, the *in situ* GISAXS study of Wirth et al. [18] on CNT grown through a two-step process using a Fe catalyst film indicates the formation of either metallic Fe or Fe_3C as the catalyst phase, such variation being attributed to the practically unavoidable residual carbon contamination present in standard CVD reactors. For our AACCVD process involving the reactor feeding with both catalyst and carbon precursors, Fe_3C phase was always found to be at the origin of VACNT, which suggests good reproducibility and robustness of this process.

In summary, our *in situ* and time-resolved WAXS experiments provide a statistical analysis of the CNT nucleation and growth process, and show that CNT growth is initiated from iron carbide nanoparticles and that the continuous feeding of the reactor with catalyst precursor involves the formation, from the Fe_3C catalyst particle located at the CNT base, of a secondary iron-based phase (γ-Fe), entrapped inside CNT.

3.2. *CNT alignment*

As mentioned above, diffraction from the regularly-spaced curved-graphene walls forming MWCNT gives rise to a characteristic peak located at $Q = 1.81$ Å^{-1} ($Q = 2\pi/d$, d being the average distance between the walls). It can be clearly seen in Fig. 2 that the intensity along the 002 ring is much more important in the horizontal direction than in the vertical one. Such angular modulation of 002 peak intensity reflects the preferential alignment of CNT along the vertical direction, perpendicularly to the silicon wafer [37]. It can be quantified using the model developed in Ref. [56]. Fitting the angular modulation along the 002 diffraction ring, as detailed in Supplementary information and illustrated in Fig. S2, allows one to determine the orientation distribution function of CNT in direct space. One, thus, calculates the order parameter defined as $\eta = \frac{1}{2}(3\langle\cos^2(\beta)\rangle - 1)$, where β is the angle between the normal to the silicon wafer (the carpet basis) and a nanotube. This order parameter is equal to 1 if all nanotubes are perfectly aligned along the normal to the carpet basis and to 0 for random orientations. Its evolution as a function of time, during precursor injection, is reported in Fig. 6, for high and low injection rates. Moreover, the determination of the orientational distribution function of the nanotubes allowed us to calculate the integrated intensity of the 002 peak, as detailed in Supplementary information. This integrated intensity is also reported in Fig. 6. It quantifies the amount of MWCNT, which is the number of nanotubes, their number of walls and their length. Fig. 6 clearly shows that global nanotube alignment improves as they grow. In the case of high injection rate (Fig. 6(a)), the order parameter η abruptly increases as soon as CNT are detected and it reaches a plateau before the end of the precursor injection, while the amount of CNT continues to increase. The saturation value of the order parameter to 0.85 proves the particularly good alignment of CNT. On the contrary, for the low injection rate (Fig. 6(b)), no saturation of the order parameter is observed during CNT growth until injection is stopped, showing that CNT continue to orientate better as they grow all along the precursor injection duration. Let us also point out that at the early beginning of nanotube growth, the order parameter is found equal to zero for the low injection rate (Fig. 6(b), inset). Indeed, the 002 intensity displayed the same intensity vertically and horizontally (isotropic signal). In agreement with these *in situ* results about the CNT alignment as a function of time, we observed by SEM a worse CNT alignment at the top of the carpet (beginning of the growth because of the base-growth mechanism) than in the lower part of the carpet.

In the literature, to the best of our knowledge, the only *in situ* analysis that could compare to the present one was published by Meshot and co-workers [27]. These authors studied the nanotube alignment using small angle X-ray scattering (SAXS). They calculated the order parameter from the angular modulation of the small wave-vector scattering signal, characteristic of the CNT, at $Q = 0.08$ Å^{-1}. The calculations detailed in Supplementary material give a more rigorous description of nanotube orientations, but Meshot's approach, where the orientational distribution function is considered to be very similar to the scattered intensity distribution, is

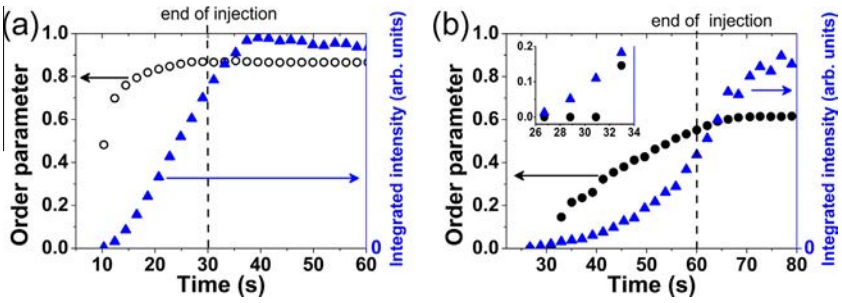

Fig. 6 – Evolution of the alignment of CNT as a function of time for the (a) high and (b) low injection rates (0.53 and 0.27 g/min). The beginning of injection corresponds to time = 0 s. The evolution of the integrated intensity of the 002 MWCNT peak as a function of time is represented by blue triangles. (A color version of this figure can be viewed online.)

widely used in the literature [57]. *In situ* experiments in Ref. [27] are performed in different conditions from the present ones, for a two-step CVD synthesis process, but they also clearly evidence the increase of CNT alignment during their growth.

A recurrent question in the literature is the one of the control of CNT alignment in carpets, as discussed in Refs. [27,58,59], to cite only a few of them. CNT interact through van der Waals interactions, which depend on (a) the distance between nanotubes *i.e.* the number of nanotubes per unit of surface in the plane of the carpet base (CNT surface density), (b) their diameters and their number of walls, and (c) their length, as discussed by He and co-workers [60]. Xu and co-workers [59], as well as Meshot et al. [27], pointed towards the relation between CNT alignment and catalyst surface density. Syntheses performed for low and high injection rates in the present *in situ* experiments led to CNT with similar internal and external mean diameters of 8 and 30 nm respectively, as was measured by *ex situ* TEM analyses, and thus with the same number of walls. The increase of the injection rate leads to an increase of the number of nucleation sites and growth of iron-based particles as evidenced in Ref. [31]. High injection rate synthesis thus leads to denser carpets of CNT with larger surface density. This result has been corroborated with our SEM observations. Samples obtained at high and low injection rates present identical nanotubes in terms of diameters, but which are more densely packed for high injection rate. We report in Fig. 7 the evolution of the orientational order parameter as a function of CNT length for the two injection rates. CNT length was obtained from the integrated intensity of the 002 peak (see calculation in Supplementary material) times the final length of the CNT in the corresponding VACNT carpets (carpet thickness measured by SEM) normalized by the integrated intensity of the 002 peak at the end of injection. Note that this calculation assumes constant CNT diameters and carpet surface density, which may not be exact at the early beginning of growth, leading to an underestimation of CNT length at the beginning of growth. Nonetheless, two distinct behaviors can be distinguished in Fig. 7, for both low and high injection rates.

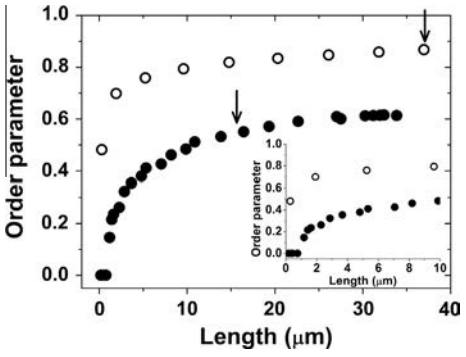

Fig. 7 – (a) Evolution of the order parameter as a function of the carpet length for the two injection rates (high injection rate, 0.53 g/min: empty circles and low one, 0.27 g/min: black dots), during the CNT growth. Arrows indicate the end of the injection in both cases. (Inset) zoom of this evolution for the first micrometers of the carpet showing for the low injection rate non-oriented MWCNT.

The orientational order parameter increases strongly with the CNT length up to a critical length value of a few μm, after which its increase is significantly reduced. The first regime clearly illustrates the cooperative nature of the alignment process and the critical role of CNT length. An additional parameter to consider is the surface density of the nanotubes. The increase of the order parameter with length in the first regime is more important for high injection rate than for low injection one, that is for larger CNT surface density. Therefore, both length and CNT surface density are shown to play a key role in CNT alignment in carpet, with increased alignment for longer nanotubes and with values of the order parameter as a function of CNT length controlled by the CNT surface density.

4. Conclusions

We have performed *in situ* time-resolved Wide Angle XRD experiments (in transmission geometry) using a prototype CVD equipment relevant for the large scale production of VACNT. This study provides new insights for the better understanding of catalyzed VACNT growth which is of great concern for the whole community of CNT synthesis.

It has been shown that crystalline cementite Fe_3C appears before CNT and that Fe_3C nanoparticles are certainly at the origin of CNT nucleation and growth. Clear correlation between the rate of the continuous carbon and iron precursor injection and the possible transformation of Fe_3C into γ-Fe and C, leading to γ-Fe nanowires which continuously detach from the mother particle at CNT base and are finally entrapped all along the CNT core, has been established. In full agreement with our experimental results, obtained for two different precursor injection rates, a plausible scenario for nanotubes nucleation, from cementite-based nanoparticle, and for their growth, concomitant with nanowires formation inside, has thus been proposed. Moreover, progressive CNT alignment has been studied quantitatively for the two injection rates used. We demonstrate that the alignment of the nanotubes varies rapidly with the nanotube length up to a critical length and that for a given carpet height, the crucial parameter is the CNT surface density which is controlled by the precursor injection rate.

Acknowledgements

We acknowledge the French National Agency of Research (ANR-ALUCINAN, reference: ANR-07-NANO-014) and RTRA-Triangle de la Physique for Alucinan Project, for funding the project and for post-doctorate financial support. We are very thankful to the Region Ile de France for the FEG-SEM financial support and to CEA-DSV (TEM platform) for TEM observation facilities. Participation of Julien Cambedouzou, Denis Petermann and Gilles Guillier at different stages of the project is also gratefully acknowledged. We also thank Stephanie Hustache for technical assistance on the XPAD detector and Fabien Legrand of the CRISTAL beamline staff for assistance during the set-up of the in-situ CVD reactor on the beamline.

Appendix A. Additional experimental details

Carbon nanotube synthesis

VACNT carpets are synthesized by AACCVD from toluene and ferrocene precursors. Briefly, the precursor mixture is made with ferrocene (2.5 wt%) dissolved in toluene and the resulting solution is injected continuously through an aerosol and carried by a helium flow (1.5 L/min) inside the reactor. The highest injection rate used was 0.53 g/min and the lowest one, obtained by reducing the injection frequency, was 0.27 g/min. Considering the He flow rate, the internal diameter of the reactor and the distance between the injection head to the center of the reactor where the substrate is placed (16 mm and 450 mm respectively), the reactive vapor needs about 4 s to reach the center of the reactor after the beginning of the precursor injection. To perform *in situ* experiments using XRD we have developed specific reactor and furnace. Aerosols are continuously injected inside the reactor placed in the furnace (see injection and exhaust paths in Fig. 1). XRD measurement requirements imposed the creation of a large exit window while keeping a homogeneous temperature inside the furnace for the respect of the VACNT nucleation and growth steps. The best compromise we found was an L-shape exit window for X-rays, allowing measurements in two directions of interest in reciprocal space (Fig. 2(a)). The sample holder, heated by the furnace, is equipped with two motors allowing fine tuning of the position and orientation of the sample in the X-ray beam. As it is illustrated in Fig. 1, the dimensions of the reactor and furnace developed for *in situ* experiments are similar to those of synthesis set-ups commonly used in laboratory allowing therefore the study of CNT growth mechanisms representative of the ones occurring in standard laboratory CVD set-ups. Syntheses were performed on thin silicon wafers (10 μm) that are stick to specific ceramic sample holders placed at the tip of a system transferring and rotating the sample in the furnace (Fig. 1).

X-ray diffraction

Experiments were performed on CRISTAL beamline at Synchrotron SOLEIL with photons of energy 17.1 keV (selected by means of a double Si(1 1 1) monochromator), giving access to wave-vectors up to 5 $Å^{-1}$. Beam size is FWHM 0.8 mm (horizontally) × 0.2 mm (vertically). The *in situ* set up was mounted on the base of 6 circles goniometer of the beamline. Alignment of the furnace/sample in the beam was performed using the available translations of the base coupled to sample (Si substrate) position adjustment with the translation and rotation stages of the motorized sample holder. The sample-detector distance was determined using a standard CeO_2 powder (SRM 674a) from NIST. Time resolved XRD experiments have been possible thanks to the use of an intense synchrotron X-ray beam combined with a prototype hybrid pixel area detector [33, 34]. The characteristics of this two-dimensional (2D) detector are very attractive in terms of fast readout time, high dynamic range, low noise and high signal-to-noise ratio allowing us to perform time-resolved measurements of very weak scattered signals during the nucleation and the growth of MWCNT carpets. The acquisition time of 1 s was set in order to detect the weak scattering signal from the small quantity of matter under investigation. Calibration and corrections of the diffraction images are presented in details in Ref. [34].

Electron microscopy

CNT carpets have been observed by *ex situ* scanning electron microscopy observations (FEGSEM, Carl Zeiss Ultra 55) in order to confirm the CNT growth on substrates and their general morphology, arrangement, cleanliness, length and density. Transmission electron microscopy (Philips CM12 and CM20 TEM) was used to analyze individual nanotubes after dispersion in ethanol and to determine their average diameters and the location, size and shape of the metal-based particles (at CNT base or inside). Thus VACNT collected carpets were gently dispersed using short ultrasonic treatment in ethanol so that the global alignment degree of the carpets could be kept even on the TEM grid which facilitates base or top tracking of the aligned CNT carpet.

REFERENCES

[1] De Volder MFL, Tawfick SH, Baughman RH, Hart AJ. Carbon nanotubes: present and future commercial applications. Science 2013;339:535–9. http://dx.doi.org/10.1126/science.1222453.

[2] Holt JK, Park HG, Wang Y, Stadermann M, Artyukhin AB, Grigoropoulos CP, et al. Fast mass transport through sub-2-nanometer carbon nanotubes. Science 2006;312:1034–7. http://dx.doi.org/10.1126/science.1126298.

[3] Baek Y, Kim C, Seo DK, Kim T, Lee JS, Kim YH, et al. High performance and antifouling vertically aligned carbon nanotube membrane for water purification. J Membr Sci 2014;460:171–7. http://dx.doi.org/10.1016/j.memsci.2014.02.042.

[4] Esconjauregui S, Fouquet M, Bayer BC, Ducati C, Smajda R, Hofmann S, et al. Growth of ultrahigh density vertically aligned carbon nanotube forests for interconnects. ACS Nano 2010;4(12):7431–6. http://dx.doi.org/10.1021/nn1025675.

[5] Ajayan M, Tour JM. Nanotube composites. Nature 2007;447:1066–8. http://dx.doi.org/10.1038/4471066a.

[6] Marconnet AM, Yamamoto N, Panzer MA, Wardle BL, Goodson KE. Thermal conduction in aligned carbon nanotube-polymer nanocomposites with high packing density. ACS Nano 2011;5(6):4818–25. http://dx.doi.org/10.1021/nn200847u.

[7] Singh C, Shaffer MS, Windle AH. Production of controlled architectures of aligned carbon nanotubes by an injection chemical vapour deposition method. Carbon 2003;41:359–68.

[8] Zhang XF, Cao AY, Wei BQ, Li YH, Wei JQ, Xu CL, et al. Rapid growth of well-aligned carbon nanotube arrays. Chem Phys Lett 2002;362:285–90.

[9] Murakami Y, Chiashi S, Miyauchi Y, Hu MH, Ogura M, Okubo T, et al. Growth of vertically aligned single-walled carbon nanotube films on quartz substrates and their optical anisotropy. Chem Phys Lett 2004;385: 298–303.
[10] Noda S, Hasegawa K, Sugime H, Kakehi K, Zhang Z, Maruyama S, et al. Millimeter-thick single-walled carbon nanotube forests: hidden role of catalyst support. Jpn J Appl Phys Lett 2007;46:L399–401. http://dx.doi.org/10.1143/JJAP.46.L399.
[11] Zhong G, Warner JH, Fouquet M, Robertson AW, Chen B, Robertson J. Growth of ultrahigh density single-walled carbon nanotube forests by improved catalyst design. ACS Nano 2012;6(4):2893–903. http://dx.doi.org/10.1021/nn203035x.
[12] Sugime H, Noda S. Millimeter-tall single-walled carbon nanotube forests grown from ethanol. Carbon 2010;48:2203–11. http://dx.doi.org/10.1016/j.carbon.2010.02.024.
[13] Zhang Q, Huang JQ, Zhao MQ, Qian WZ, Wei F. Carbon nanotube mass production: principles and processes. Chem Sus Chem 2011;4:864–89. http://dx.doi.org/10.1002/cssc.201100177.
[14] Zhang Q, Huang JQ, Zhao MQ, Qian WZ, Wei F. Modulating the diameter of carbon nanotubes in array via floating catalyst chemical vapour deposition. Appl Phys A 2009;94:853–60. http://dx.doi.org/10.10007/s00339-008-4904-5.
[15] Hofmann S, Sharma R, Ducati C, Du G, Mattevi C, Cepek C, et al. *In situ* observations of catalyst dynamics during surface-bound carbon nanotube nucleation. Nano Lett 2007;7:602–8. http://dx.doi.org/10.1021/nl0624824.
[16] Rodriguez-Manzo JA, Terrones M, Terrones H, Kroto HW, Sun L, Banhart F. *In situ* nucleation of carbon nanotubes by the injection of carbon atoms into metal particles. Nat Nanotechnol 2007;2:307–11. http://dx.doi.org/10.1038/nnano.2007.107.
[17] Yoshida H, Takeda S, Uchiyama T, Kohno H, Homma Y. Atomic-scale *in situ* observation of carbon nanotube growth from solid state iron carbide nanoparticles. Nano Lett 2008;8(7):2082–6. http://dx.doi.org/10.1021/nl080452q.
[18] Wirth CT, Bayer BC, Gamalski AD, Esconjauregui S, Weatherup RS, Ducati C, et al. The phase of iron catalyst nanoparticles during carbon nanotube growth. Chem Mater 2012;24(24):4633–40. http://dx.doi.org/10.1021/cm301402g.
[19] Picher M, Anglaret E, Arenal R, Jourdain V. Self-deactivation of single-walled carbon nanotube growth studied by *in situ* Raman measurements. Nano Lett 2009;9(2):542–7. http://dx.doi.org/10.1021/nl802661z.
[20] Chiashi S, Murakami Y, Miyauchi Y, Maruyama S. Cold wall CVD generation of single- walled carbon nanotubes and *in situ* Raman scattering measurements of the growth stage. Chem Phys Lett 2004;386:89–94. http://dx.doi.org/10.1016/j.cplett.2003.12.126.
[21] Sharma R, Iqbal Z. *In situ* observations of carbon nanotube formation using environmental transmission electron microscopy. Appl Phys Lett 2004;84:990–2. http://dx.doi.org/10.1063/1.1646465.
[22] Oshima H, Shimazu T, Siry M, Ko M. Analysis of Fe catalyst during carbon nanotube synthesis by Mossbauer spectroscopy. J Phys Chem C 2009;113(43):18523–6. http://dx.doi.org/10.1021/jp905195b.
[23] Pinheiro JP, Schouler MC, Dooryhee E. In situ X-ray diffraction study of carbon nanotubes and filaments during their formation over Co/Al2O3 catalysts. Solid State Commun 2002;123:161–6 [PII: S0038-1098(02)00189-8].
[24] Nishimura K, Okazaki N, Pan LJ, Nakayama Y. *In situ* study of iron catalysts for carbon nanotube growth using X-ray diffraction analysis. Jpn J Appl Phys Lett 2004;43:1–4.
[25] Emmenegger C, Bonard JM, Mauron P, Sudan P, Lepora A, Grobety B, et al. Synthesis of carbon nanotubes over Fe Catalyst on aluminium and suggested growth mechanism. Carbon 2003;41:539–47 [PII: S0008-6223(02)00362-7].
[26] Einarsson E, Murakami Y, Kadowaki M, Maruyama S. Growth dynamics of vertically aligned single-walled carbon nanotubes from *in situ* measurements. Carbon 2008;46:923–30. http://dx.doi.org/10.1016/j.carbon.2008.02.021.
[27] Meshot ER, Verploegen E, Bedewy M, Tawfick S, Woll AR, Green KS, et al. High-speed *in situ* X-ray scattering of carbon nanotube film nucleation and self-organization. ACS Nano 2012;6(6):5091–101. http://dx.doi.org/10.1021/nn300758f.
[28] Puretzky AA, Geohegan DB, Jesse S, Ivanov IN, Eres G. *In situ* measurements and modeling of carbon nanotube array growth kinetics during chemical vapor deposition. Appl Phys A 2005;81(2):223–40. http://dx.doi.org/10.1007/s00339-005-3256-7.
[29] Kuznetsov VL, Krasnikov DV, Schmakov AN, Elumeeva K. *In-situ* and *ex-situ* time resolved study of multi-component Fe-Co oxide catalyst activation during MWCNT synthesis. Phys Status Solidi B 2012;249(12):2390–4. http://dx.doi.org/10.1002/pssb.201200120.
[30] Pinault M, Pichot V, Khodja H, Launois P, Reynaud C, Mayne-L'Hermite M. Evidence of sequential lift in growth of aligned multiwalled carbon nanotube multilayers. Nano Lett 2005;5(12):2394–8. http://dx.doi.org/10.1021/nl051472k.
[31] Castro C, Pinault M, Coste-Leconte S, Porterat D, Bendiab N, Reynaud C, et al. Dynamics of catalyst particle formation and multi-walled carbon nanotube growth in aerosol-assisted catalytic chemical vapor deposition. Carbon 2010;48:3807–16. http://dx.doi.org/10.1016/j.carbon.2010.06.045.
[32] Landois P, Rouzière S, Pinault M, Porterat D, Mocuta C, Elkaim E, et al. Growth of aligned multi-walled carbon nanotubes: first *in situ* and time-resolved X-ray diffraction analysis. Phys Status Solidi B 2011;248(11):2449–53. http://dx.doi.org/10.1002/pssb.201100201.
[33] Medjoubi K, Bucaille T, Hustache S, Berar JF, Boudet N, Clemens JC, et al. Detective quantum efficiency, modulation transfer function and energy resolution comparison between CdTe and silicon sensors bump-bonded to XPAD3S. J Synchrotron Radiat 2010;17(4):486–95. http://dx.doi.org/10.1107/S0909049510013257.
[34] Le Bourlot C, Landois P, Djaziri S, Renault PO, Le Bourhis E, Goudeau P, et al. Synchrotron X-ray diffraction experiments with a prototype hybrid pixel detector. J Appl Crystallogr 2012;45:38–47. http://dx.doi.org/10.1107/S0021889811049107.
[35] Pinault M, Mayne-L'Hermite M, Reynaud C, Pichot V, Launois P, Ballutaud D. Growth of multiwalled carbon nanotubes during the initial stages of aerosol-assisted CCVD. Carbon 2005;14:2968–76. http://dx.doi.org/10.1016/j.carbon.2005.06.011.
[36] Heresanu V, Castro C, Cambedouzou J, Pinault M, Stephan O, Reynaud C, et al. Nature of the catalyst particles in CCVD synthesis of multiwalled carbon nanotubes revealed by the cooling step study. J Phys Chem C 2008;112(19):7371–8. http://dx.doi.org/10.1021/jp709825y.
[37] Pichot V, Launois P, Pinault M, Mayne-L'Hermite M, Reynaud C. Evidence of strong nanotube alignment and for iron preferential growth axis in multiwalled carbon nanotube carpets. Appl Phys Lett 2004;85(3):473–5. http://dx.doi.org/10.1063/1.1773611.
[38] Sajitha EP, Prasad V, Subramanyam SV, Eto S, Takai K, Enoki T. Synthesis and characteristics of iron nanoparticles in a carbon matrix along with the catalytic graphitization of amorphous carbon. Carbon 2004;42:2815–20. http://dx.doi.org/10.1016/j.carbon.2004.06.027.

[39] Rice GW, Miseo S, Soled SL. Laser produced iron carbide-based catalysts. U.S. Patent 4,687,753, August 18, 1987.
[40] Zhang J, Schneider A, Inden G. Characterisation of the coke formed during metal dusting of iron in CO–H_2–H_2O gas mixtures. Corros Sci 2003;45(6):1329–41. http://dx.doi.org/10.1016/S0010-938X(02)00251-2.
[41] Wei Q, Pippel E, Woltersdorf J, Grabke HJ. Microprocesses of coke formation in metal dusting. Mater Corros 1999;50(11):628–33. http://dx.doi.org/10.1002/(SICI)1521-4176(199911)50:1.
[42] Conejo AN, Martins GP. Conversion of hematite to iron carbides by gas phase carbidization. ISIJ Int 1997;37(10):967–76.
[43] Sacco A, Thacker P, Chang TN, Chiang ATS. The initiation and growth of filamentous carbon from α-iron in H_2, CH_4, H_2O, CO_2, and CO gas mixtures. J Catal 1984;85:224–36 [DOI: 0021-9517/84].
[44] Debokx PK, Kock A, Boellaard E, Klop W, Geus JW. The formation of filamentous carbon on iron and nickel catalysts: I. Thermodynamics. J Catal 1985;96:454–67 [DOI: 0021-9517/8].
[45] Behr MJ, Mkhoyan KA, Aydil ES. Orientation and morphological evolution of catalyst nanoparticles during carbon nanotube growth. ACS Nano 2010;4(9):5087–94. http://dx.doi.org/10.1021/nn100944n.
[46] He Z, Maurice JL, Gohier A, Lee CS, Pribat D, Cojocaru CS. Iron catalysts for the growth of carbon nanofibers: Fe, Fe_3C or Both? Chem Mater 2011;23(24):5379–87. http://dx.doi.org/10.1021/cm202315j.
[47] Perez-Cabero M, Taboada JB, Guerrero-Ruiz A, Overweg AR, Rodriguez-Ramos I. The role of alpha-iron and cementite phases in the growing mechanism of carbon nanotubes: a Fe-57 Mossbauer Spectroscopy Study. Phys Chem Chem Phys 2006;8:1230–5. http://dx.doi.org/10.1039/b516243b.
[48] Sharma R, Moore E, Rez P, Treacy MMJ. Site-specific fabrication of Fe particles for carbon nanotube growth. Nano Lett 2009;9(2):689–96. http://dx.doi.org/10.1021/nl803180e.
[49] Schaper AK, Hou HQ, Greiner A, Phillipp F. The role of iron carbide in multiwalled carbon nanotube growth. J Catal 2004;222:250–4. http://dx.doi.org/10.1016/j.jcat.2003.11.011.
[50] Kim H, Sigmund W. Iron particles in carbon nanotubes. Carbon 2005;43:1743–8. http://dx.doi.org/10.1016/j.carbon.2005.02.019.
[51] Zhang J, Ostrovski O. Cementite formation in CH_4–H_2–Ar gas mixture and cementite stability. ISIJ Int 2001;41(4):333–9.
[52] Xiang R, Luo G, Qian W, Zhang Q, Wang Y, Wei F, et al. Encapsulation, compensation, and substitution of catalyst particles during continuous growth of carbon nanotubes. Adv Mater 2007;19(17):2360–3. http://dx.doi.org/10.1002/adma.200602468.
[53] Pigos E, Penev E, Ribas MA, Sharma R, Yakobson BI, Harutyunyan AR. Carbon nanotube nucleation driven by catalyst morphology dynamics. ACS Nano 2011;5(12):10096–101. http://dx.doi.org/10.1021/nn2040457.
[54] Cao AY, Zhang XF, Wei JQ, Li YH, Xu CL, Liang J, et al. Macroscopic three-dimensional arrays of Fe nanoparticles supported in aligned carbon nanotubes. J Phys Chem B 2001;105(48):11937–40. http://dx.doi.org/10.1021/jp0127521.
[55] Kock A, Debokx PK, Boellaard E, Klop W, Geus JW. The formation of filamentous carbon on iron and nickel catalysts: II. Mechanism. J Catal 1985;96:468–80 [DOI: 0021-9517/85].
[56] Pichot V, Badaire S, Albouy P, Zakri C, Poulin P, Launois P. Structural and mechanical properties of single-wall carbon nanotube fibers. Phys Rev B 2006;74:245416–8 [DOI: 1098-0121/2006/74(24)/245416(8)].
[57] Hermans PH. Contribution to the physics of cellulose fibres: a study in sorption, density, refractive power and orientation. Amsterdam: Elsevier Pub. Co.; 1946.
[58] Fan SS, Chapline MG, Franklin NR, Tombler TW, Cassell AM, Dai HJ. Self-oriented regular arrays of carbon nanotubes and their field emission properties. Science 1999;283:512–4. http://dx.doi.org/10.1126/science.283.5401.512.
[59] Xu M, Futaba DN, Yumura M, Hata K. Alignment control of carbon nanotube forest from random to nearly perfectly aligned by utilizing the crowding effect. ACS Nano 2012;6(7):5837–44. http://dx.doi.org/10.1021/nn300142j.
[60] He D, Bozlar M, Genestoux M, Bai J. Diameter- and length-dependent self-organizations of multi-walled carbon nanotubes on spherical alumina microparticles. Carbon 2010;48:1159–70. http://dx.doi.org/10.106/j.carbon.2009.11.039.